High-Accuracy Waveguide Leaky-Mode Analysis Using a Multidomain Pseudospectral Frequency-Domain Method Incorporated With Stretched Coordinate PML

Chih-Yu Wang, Hsuan-Hao Liu, Shih-Yung Chung, Chun-Hao Teng, Chung-Ping Chen, *Member, IEEE*, and Hung-chun Chang, *Senior Member, IEEE, Fellow, OSA*

***Abstract*—A recently developed pseudospectral frequency-domain (PSFD) method employing a penalty scheme is further incorporated with stretched coordinate perfectly matched layers (PMLs) in order to solve waveguide leaky modes. Several standard leaky-mode slab and circular waveguides, including the W-type and M-type ones, are examined first by solving their complex effective indexes and field profiles, showing that the PSFD method achieves computational accuracy on the order of 10^{-15}. Then, this high-accuracy solver is used to analyze waveguide structures with more complicated geometries, such as the leaky six-air-hole fiber, for which self convergence of accuracy in calculated effective indexes is demonstrated to be on the orders of 10^{-14}, and two rectilineal waveguides with sharp corners, i.e., the rib waveguide and the photonic wire. Comparison of the PSFD method obtained results for these more complicated waveguide structures with those from other methods in the literature is presented and discussed.**

***Index Terms*—Leaky waveguide modes, optical waveguide analysis, pseudospectral frequency domain (PSFD) method.**

I. Introduction

GENERALLY, optical wave-guiding mechanisms based on total internal reflection [1], photonic band gap effect [2]–[4], and antiresonant reflection [5]–[7] have been mostly adopted. However, imperfect field confinement in the guiding region might occur in certain waveguide structures functioned by these mechanisms, resulting in leaky modes with confinement losses. Physically, leaky modes are known not members of a complete set of orthogonal basis functions, and behave analogy to the tunneling effect in quantum physics [8], [9] that most wave powers are longitudinally guided inside the core but portions are laterally propagating in the outermost layer. The most specific characteristics of the leaky mode are therefore its complex propagation constant and infinite field magnitude at the infinite transverse spatial limit [9], because longitudinal decay would lead to increase of fields in the transverse direction according to the relationship between wavenumber and propagation constant [10]. Therefore, an accurate computational method implemented with well-functioning absorbing mechanism such as using the perfectly matched layers (PMLs) [11] is essential for solving waveguide leaky modes with such field profiles.

In analyzing waveguides, modal characteristics including field profiles, propagation constants, effective indexes, modal (confinement) losses, and dispersion curve are mainly concerned, and the effective index which is defined as the propagation constant divided by the free-space wavenumber is usually chosen as an indicator for assessing the computation accuracy of a method. Optical waveguide leaky-mode solvers have been developed, in particular after the invention of holey fibers or photonic crystal fibers [2]–[4], based on different numerical methods, such as the finite difference method [12]–[14], the finite element method [15], [16], the multipole method [17], [18], the boundary integral equation method [19], the pseudospectral frequency-domain (PSFD) method [20], [21], etc. This paper concerns further development of the pseudospectral method which is based on the high-order Legendre or Chebyshev interpolation basis and can then provide exponentially converged computation accuracy with respect to the grid resolution [22], [23]. Prior PSFD mode solvers have been formulated using second-order Helmholtz equations [20]–[23] and demonstrated to provide excellent numerical accuracy in eigenmode analysis.

Recently, an alternate PSFD method with a penalty scheme was developed [24], which shows 10^{-15} accuracy in solving the modal effective indexes for standard metallic and fiber waveguides. Different from above-mentioned Helmholtz equations-based methods, this newly reported PSFD method is formulated on the first-order differential equations written from both curl and divergence laws in Maxwell equations

Manuscript received August 24, 2012; revised March 15, 2013; accepted April 30, 2013. Date of publication May 31, 2013; date of current version June 19, 2013. This work was supported in part by the National Science Council of the Republic of China under Grants NSC100-2628-M-002-008 and NSC99-2221-E-002-107-MY2, in part by the Excellent Research Projects of National Taiwan University under grant 101R89081, and in part by the Ministry of Education of the Republic of China under "The Aim of Top University Plan" grant.

C. Y. Wang, S. Y. Chung, and C. P. Chen are with the Graduate Institute of Electronics Engineering and the Department of Electrical Engineering, National Taiwan University, Taipei 10617, Taiwan.

H. H. Liu is with the Graduate Institute of Photonics and Optoelectronics, National Taiwan University, Taipei 10617, Taiwan.

C. H. Teng is with the Department of Applied Mathematics and Center of Mathematical Modeling and Scientific Computing, National Chiao Tung University, Hsinchu 30010, Taiwan.

H. C. Chang is with the Department of Electrical Engineering, the Graduate Institute of Photonics and Optoelectronics, and the Graduate Institute of Communication Engineering, National Taiwan University, Taipei 10617, Taiwan (e-mail: hcchang@cc.ee.ntu.edu.tw).

Color versions of one or more of the figures in this paper are available online at http://ieeexplore.ieee.org.

Digital Object Identifier 10.1109/JLT.2013.2265554

[26]. Besides, the multidomain scheme is employed in the formulation, with which the computational domain is divided into suitable number of curvilinear sub-domains [25] such that the shapes of the waveguide structure interfaces can fit the sub-domain boundaries, facilitating accurate fulfillment of the field continuity conditions across the interfaces. In this paper, this new method is adopted and implemented with the stretched coordinate PML [27], [28], which is quite suitable for first-order equations, for solving waveguide leaky modes with high accuracy. We will show in the numerical examples that the inclusion of the stretched coordinate PML still maintains high accuracy of the PSFD method, and the position where the PML region is placed has negligible effect on the computation accuracy, even for waveguides with no need in effective indexes of the PML like the fiber waveguide. It will be shown that this PSFD solver can achieve 10^{-15}–10^{-14} numerical accuracy for solving leaky-mode waveguide structures without singular-field corners. In comparison of our PSFD solution for a leaky six-air-hole fiber [17] with that from a recently reported new high-order boundary-integral-equation (BIE) method [19] which was shown to achieve exponential convergence and extremely high accuracy, it is found that the agreement in the calculated effective index is to the order of 10^{-13} for both the real and imaginary parts. The PSFD analysis will then be applied to the conventional rib waveguide [29] and the more complicated photonic wire [30] for which the application of the BIE method would become more difficult.

The rest of this paper is organized as follows. The governing Maxwell's equations with the penalty scheme, the implementation of the stretched coordinate PML, and the eigenmode solver formulation are described in Section II. The Legendre pseudospectral method is introduced in Section III. Then, numerical examples are given and discussed in Section IV, where several one-dimensional (1-D) (slab) and 2-D (circular) leaky-mode waveguides, including W-type [9], [31] and M-type [5], [6] waveguides, are analyzed first, followed by the examination of the more complicated 2-D structures such as the six-air-hole fiber and the photonic wire. The conclusion is drawn in Section V.

II. Physical Equations, PML, and Penalty-Scheme Formulation

In a source-free and linear isotropic medium with permittivity ε and permeability μ, the time-harmonic Maxwell's curl and divergent equations for frequency-domain computation are written as

$$\nabla \times \mathbf{E} = -j\omega\,\mu\mathbf{H} \tag{1a}$$

$$\nabla \times \mathbf{H} = j\omega\varepsilon\mathbf{E} \tag{1b}$$

$$\nabla \cdot (\varepsilon\mathbf{E}) = 0 \tag{1c}$$

$$\nabla \cdot (\mu\mathbf{H}) = 0 \tag{1d}$$

where ω is the angular frequency. Without loss of generality, waves are considered to propagate along the z-axis in the waveguide, i.e., no structural variations along the z direction. Therefore, spatial derivative with respect to z becomes $\partial/\partial z = -j\beta$, where β is the modal propagation constant. For convenience, we normalize the magnetic field $\mathbf{H}$ to $\sqrt{\varepsilon_0/\mu_0}\mathbf{H}$.

Traditionally, waveguide modes are solved by second order Helmholtz equations, like in [23]. A new PSFD method has been recently developed in [24] using first order formulations instead, which we adopt in this paper as well. In brief, two of the eight equations in (1) without $j\beta$ terms are removed, i.e.,

$$-jk_0H_y + \frac{\partial E_z}{\partial x} = j\beta E_x \tag{2a}$$

$$jk_0H_x + \frac{\partial E_z}{\partial y} = j\beta E_y \tag{2b}$$

$$-\frac{\partial E_x}{\partial x} - \frac{\partial E_y}{\partial y} = j\beta E_z \tag{2c}$$

$$jk_0\varepsilon_r E_y + \frac{\partial H_z}{\partial x} = j\beta H_x \tag{2d}$$

$$-jk_0\varepsilon_r E_x + \frac{\partial H_z}{\partial y} = j\beta H_y \tag{2e}$$

$$-\frac{\partial H_x}{\partial x} - \frac{\partial H_y}{\partial y} = j\beta H_z. \tag{2f}$$

These six equations lead to an eigen-problem in the form, $\tilde{A}\tilde{x} = \lambda\tilde{x}$, for solving waveguide modes, with $\tilde{A}$ containing the differential operators, the eigenvalue λ equal to $j\beta$ to be searched, and the eigenvector $\tilde{x}$ composed of the electric and magnetic fields of the corresponding mode. This eigen-problem can be solved using efficient iterative algorithms such as the bi-conjugate gradient (BiCG) method along with the shifted inverse power method (SIPM).

For handling boundary conditions between materials, the penalty scheme as utilized in [24] is also adopted here. First, (2) can be rewritten as

$$jk_0Mq + A_x\frac{\partial q}{\partial x} + A_y\frac{\partial q}{\partial y} = j\beta A_z q \tag{3}$$

where $k_0 = \omega\sqrt{\varepsilon_0\mu_0}$, $q = [\varepsilon_r E_x, \varepsilon_r E_y, E_z, H_x, H_y, H_z]^T$, $A_z = \mathrm{diag}[1/\varepsilon_r, 1/\varepsilon_r, -\varepsilon_r, 1, 1, -1]^T$, and the elements of the matrices M, A_x, and A_y are simply 0, 1, and -1 depending on the presence of fields in (2). Next, the penalty term $P = [\delta/(2\omega_0)]S(n)\Lambda[R(n) - R^{BC}(n)]$ is added into (2). The diagonal matrix Λ is composed of the eigenvalues of the matrix $A(n)$, the matrix $S(n)$ is composed of the eigenvectors of $A(n)$, with $A(n) = n_xA_x + n_yA_y$, in which n_x and n_y are defined below, and the characteristic state vectors $R(n)$ are defined as $R(n) = S^T(n)q = [R_1, R_2, R_3, R_4, R_5, R_6]^T$ as in [24]. Considering boundary conditions at the interface between two adjacent sub-domains I and II in the multidomain approach, with the unit normal vector $\hat{n} = n_x\hat{x} + n_y\hat{y}$ perpendicular to the interface with the relationship $\hat{n} = \hat{n}^I = -\hat{n}^{II}$, where the superscripts I and II specify the sub-domains where the vectors are defined at the interface, we add R_2^{II} to R_1^I and add R_6^{II} to R_5^I with the aids of physical boundary conditions [24] and obtain

$$R_1^I + R_2^{II} = \frac{1}{\sqrt{2}}[\hat{n}\cdot(\varepsilon_r^I\bar{E}_t^I - \varepsilon_r^{II}\bar{E}_t^{II}) - (E_z^I - E_z^{II})] = 0 \tag{4a}$$

$$R_5^I + R_6^{II} = \frac{1}{\sqrt{2}}[\hat{n}\cdot(\bar{H}_t^I - \bar{H}_t^{II}) + (H_z^I - H_z^{II})] = 0. \tag{4b}$$

Equations (4a) and (4b) lead to $R_1^I = -R_2^{II}$ and $R_5^I = -R_6^{II}$, respectively, i.e., $R_1^{I^{BC}} = -R_2^{II}$ and $R_2^{I^{BC}} = -R_1^{II}$, which means that if we want to add considerations of physical boundary conditions into (2) or (3) at material interfaces of two adjacent sub-domains, we can simply place characteristic state vectors of (4) into the penalty terms. Then, after matrix multiplications of $S(n)$, Λ, and $[R(n) - R^{BC}(n)]$ in the penalty term P, the six first-order Maxwell's equations in (2) for sub-domain I, with the added P and straightforward manipulations, will become

$$-jk_0H_y^I + \frac{\partial E_z^I}{\partial x} - \frac{\delta n_x^I}{2\omega_0}\left(E_z^I - E_z^{II}\right) = j\beta E_x^I \tag{5a}$$

$$jk_0H_x^I + \frac{\partial E_z^I}{\partial y} - \frac{\delta n_y^I}{2\omega_0}\left(E_z^I - E_z^{II}\right) = j\beta E_y^I \tag{5b}$$

$$-\frac{\partial E_x^I}{\partial x} - \frac{\partial E_y^I}{\partial y} + \frac{\delta}{2\omega_0}\left[n_x^I\left(E_x^I - \frac{\varepsilon_r^{II}}{\varepsilon_r^I}E_x^{II}\right) + n_y^I\left(E_y^I - \frac{\varepsilon_r^{II}}{\varepsilon_r^I}E_y^{II}\right)\right] = j\beta E_z^I \tag{5c}$$

$$jk_0\varepsilon_r^I E_y^I + \frac{\partial H_z^I}{\partial x} - \frac{\delta n_x^I}{2\omega_0}\left(H_z^I - H_z^{II}\right) = j\beta H_x^I \tag{5d}$$

$$-jk_0\varepsilon_r^I E_x^I + \frac{\partial H_z^I}{\partial y} - \frac{\delta n_y^I}{2\omega_0}\left(H_z^I - H_z^{II}\right) = j\beta H_y^I \tag{5e}$$

$$-\frac{\partial H_x^I}{\partial x} - \frac{\partial H_y^I}{\partial y} + \frac{\delta}{2\omega_0}\left[n_x^I\left(H_x^I - H_x^{II}\right) + n_y^I\left(H_y^I - H_y^{II}\right)\right] = j\beta H_z^I \tag{5f}$$

where δ is unity when the grid point is at the boundary edge, and is zero otherwise, and ω_0 is the quadrature weight on the interface which will be defined in the next section.

For solving waveguide leaky modes, a suitable perfectly matched layer (PML) [11] is required to be implemented. The stretched coordinate PML [27], [28] is chosen in this paper because of its ease of implementation on first order equations and its outstanding ability of absorbing outward propagating waves. According to [27] and [28], the stretched coordinate PML can be implemented by simply changing partial derivatives as $\partial/\partial\tilde{x} = (1/s_x)\partial/\partial x$ and $\partial/\partial\tilde{y} = (1/s_y)\partial/\partial y$. Similarly, the vector differential operator $\tilde{\nabla}$ in the stretched coordinate becomes $\tilde{\nabla} = \tilde{x}(1/s_x)\partial/\partial x + \tilde{y}(1/s_y)\partial/\partial y$. The absorptive variables s_x and s_y are defined as $s_x = 1 + (\sigma_x)/(j\omega\varepsilon)$ and $s_y = 1 + (\sigma_y)/(j\omega\varepsilon)$ [27], [28], where σ_x and σ_y are the electric conductivities. To reduce possible undesired reflection waves, we choose suitable profiles for σ_x and σ_y such as, for example, $\sigma_x(x_i) = c((|x_i - x_0|)/(L_{PML}))^m$ along the x-axis, with the parameters c and m being free variables for adjusting performance of the PML, $|x_i - x_0|$ is the distance of the ith grid point away from the innermost interface of the PML, and L_{PML} is the length of the PML region. This is a gradually growing profile and thus its strength of absorption as the grids get deeper into the PML region. Therefore, in the PML region, (5) will become

$$-jk_0H_y^I + \frac{1}{s_x}\frac{\partial E_z^I}{\partial x} - \frac{\delta}{2\omega_0}\frac{n_x^I}{s_x}\left(E_z^I - E_z^{II}\right) = j\beta E_x^I \tag{6a}$$

$$jk_0H_x^I + \frac{1}{s_y}\frac{\partial E_z^I}{\partial y} - \frac{\delta}{2\omega_0}\frac{n_y^I}{s_y}\left(E_z^I - E_z^{II}\right) = j\beta E_y^I \tag{6b}$$

$$-\frac{1}{s_x}\frac{\partial E_x^I}{\partial x} - \frac{1}{s_y}\frac{\partial E_y^I}{\partial y} + \frac{\delta}{2\omega_0}\left[\frac{n_x^I}{s_x}\left(E_x^I - \frac{\varepsilon_r^{II}}{\varepsilon_r^I}E_x^{II}\right) + \frac{n_y^I}{s_y}\left(E_y^I - \frac{\varepsilon_r^{II}}{\varepsilon_r^I}E_y^{II}\right)\right] = j\beta E_z \tag{6c}$$

$$jk_0\varepsilon_r^I E_y^I + \frac{1}{s_x}\frac{\partial H_z^I}{\partial x} - \frac{\delta}{2\omega_0}\frac{n_x^I}{s_x}\left(H_z^I - H_z^{II}\right) = j\beta H_x^I \tag{6d}$$

$$-jk_0\varepsilon_r^I E_x^I + \frac{1}{s_y}\frac{\partial H_z^I}{\partial y} - \frac{\delta}{2\omega_0}\frac{n_y^I}{s_y}\left(H_z^I - H_z^{II}\right) = j\beta H_y^I \tag{6e}$$

$$-\frac{1}{s_x}\frac{\partial H_x^I}{\partial x} - \frac{1}{s_y}\frac{\partial H_y^I}{\partial y} + \frac{\delta}{2\omega_0}\left[\frac{n_x^I}{s_x}\left(H_x^I - H_x^{II}\right) + \frac{n_y^I}{s_y}\left(H_y^I - H_y^{II}\right)\right] = j\beta H_z^I. \tag{6f}$$

Generally, the PML is designed to absorb waves in a single direction, therefore similar σ_y profile along the y direction is used by replacing the variable x with y in $\sigma_x(x_i)$, and both σ_x and σ_y will be needed at the corner region of the PML.

III. The Legendre Pseudospectral Method Formulation

Now we discuss the Legendre pseudospectral method for numerically treating the spatial derivatives in the above governing equations. Under the multidomain scheme, each curvilinear quadrilateral sub-domain region in Cartesian coordinates (x, y) can be mapped onto a square region $[-1, 1] \times [-1, 1]$ in curvilinear coordinates (ξ, η) by using the transfinite blending function described in [25] to construct $\xi = \xi(x, y)$ and $\eta = \eta(x, y)$. Applying the chain rule, derivatives of a 2-D function $f(x, y)$ will then become

$$\frac{\partial f(x,y)}{\partial x} = \frac{\partial \xi}{\partial x}\frac{\partial f(x,y)}{\partial \xi} + \frac{\partial \eta}{\partial x}\frac{\partial f(x,y)}{\partial \eta} \tag{7a}$$

$$\frac{\partial f(x,y)}{\partial y} = \frac{\partial \xi}{\partial y}\frac{\partial f(x,y)}{\partial \xi} + \frac{\partial \eta}{\partial y}\frac{\partial f(x,y)}{\partial \eta}. \tag{7b}$$

Some properties of Legendre polynomials, which we use as the basis for the interpolation of a function, will be given below.

In the Legendre pseudospectral method, spatial arrangement of grid points is defined by the Legendre-Gauss-Lobatto (LGL) quadrature points ξ_i arranged in the interval $[-1, 1]$, which are the roots of the polynomial $(1 - \xi^2)P_N'(\xi)$ [23], [24] with the prime denoting derivative and P_N being the Legendre polynomial of degree N defined by

$$P_N(\xi) = \frac{1}{2^N N!}\frac{d^N}{d\xi^N}(\xi^2 - 1)^N. \tag{8}$$

Associated with these LGL quadrature points are a set of quadrature weights ω_i for $i = 0, 1, 2, \ldots, N$. If $f(\xi)$ is a polynomial of degree at most $2N + 1$, we have the quadrature rule [23], [24]

$$\sum_{i=0}^{N} f(\xi_i)\omega_i = \int_{-1}^{1} f(\xi)d\xi \tag{9}$$

where the quadrature weights are defined by

$$\omega_i = \begin{cases} \frac{2}{N(N+1)}, & i = 0, N \\ -\frac{2}{(N+1)} \frac{1}{P_N(\xi_i) P'_{N-1}(\xi_i)}, & \text{otherwise.} \end{cases} \quad (10)$$

Based on these LGL collocation points, one can use the degree-N Lagrange interpolation polynomials $l_j(\xi)$ as the bases to approximate an arbitrary function $f(\xi)$ such that

$$f(\xi) \approx \sum_{j=0}^{N} f(\xi_j) l_j(\xi) \quad (11)$$

where

$$l_j(\xi) = -\frac{(1-\xi^2) P'_N(\xi)}{N(N+1)(\xi - \xi_j) P_N(\xi_j)}. \quad (12)$$

Then, the derivative of the function $f(\xi)$ at the LGL quadrature point ξ_i can also be approximated as

$$\frac{df(\xi_i)}{d\xi} \approx \sum_{j=0}^{N} \frac{dl_j(\xi_i)}{d\xi} f(\xi_j) = \sum_{j=0}^{N} D_{ij} f(\xi_j). \quad (13)$$

The differential coefficient D_{ij} is defined in [23] and [24] by

$$D_{ij} = \begin{cases} -\frac{N(N+1)}{4}, & i = j = 0 \\ \frac{N(N+1)}{4}, & i = j = N \\ 0, & 0 < (i = j) < N \\ \frac{P_N(\xi_i)}{P_N(\xi_j)} \frac{1}{\xi_i - \xi_j} & i \neq j \end{cases}. \quad (14)$$

The so-called differential matrix operator with D_{ij} elements can thus be substituted into the spatial derivative in (13) as

$$\frac{\partial}{\partial \xi} = \begin{bmatrix} D_{00} & D_{01} & \cdots & D_{0N} \\ D_{10} & D_{11} & \cdots & D_{1N} \\ \vdots & \vdots & \vdots & \vdots \\ D_{N0} & D_{N1} & \cdots & D_{NN} \end{bmatrix}. \quad (15)$$

This is the key feature of the Legendre PSFD method, i.e., for the 1-D example, the derivative of $f(\xi)$ at an LGL point ξ_i in the region $[-1, 1]$ can be approximated in terms of $f(\xi)$ values at the $N+1$ LGL points in the same region. Therefore, spatial derivatives of fields in (5) and (6) can be simply replaced by this differential matrix operator D_{ij} in the $\tilde{A}\tilde{x} = \lambda \tilde{x}$ eigen-problem system, and the resultant eigen-problem becomes a sparse matrix having penalty, PML, and repeatedly appearing D_{ij} terms in the $\tilde{A}$ matrix. Note that matrix sparsity will give better computational behavior, including less memory usage and faster computation. Besides, for solving huge computations of matrix multiplication by parallel computations, we adopt hardware acceleration using the graphic processing unit (GPU) that each of multi-processors can handel one row of matrix multiplication at the same time.

In the 2-D waveguide structures to be discussed in the next section, the grid meshes based on the LGL points in each sub-domain will be plotted for a given $N = 12$. In the figures, the curved structure and the whole computational region can be seen being partitioned into curvilinear sub-domains, and $(N+1) \times (N+1)$ LGL grid points are not uniformly distributed but somewhat following the outline of the domain edges. Please note that the LGL grid points at each edge side of a sub-domain are co-located with the LGL grid points at one edge side of its adjacent sub-domain. These co-located grid points are counted as distinct sets of points, and the penalty scheme is applied on the two sets for exchanging information of boundary conditions.

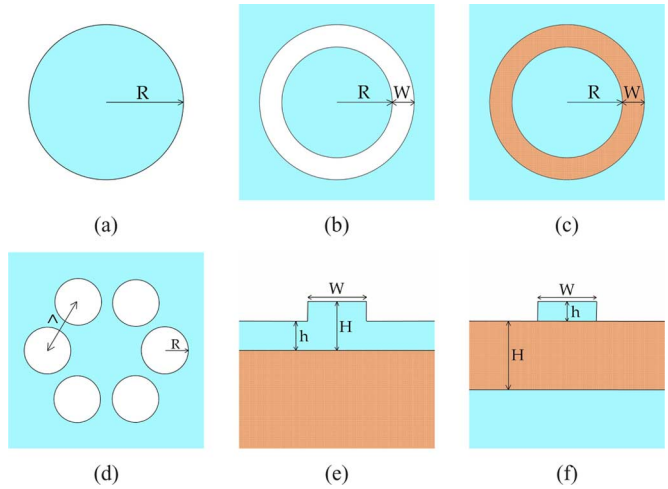

Fig. 1. 2-D waveguide geometries. (a) Circular fiber. (b) W-type fiber. (c) M-type fiber. (d) Six-air-hole fiber. (e) Rib waveguide. (f) Photonic wire.

IV. Numerical Results

In this section, we will apply our PSFD method with stretched coordinate PML to solve several standard optical waveguides. 1-D slab waveguides will be examined first, and then their corresponding 2-D fiber structures, which have circular symmetries, will be analyzed. Next, optical waveguides with more complicated structures will be analyzed, including the six-air-hole fiber [17], [18], the rib waveguide [29], and the photonic wire waveguide [30]. The latter two are with sharp dielectric corners at which electric-field singularities might exist, and how such sharp corners would affect the accuracy of computation will be discussed. The cross-sections of the 2-D structures to be discussed in this section are depicted in Fig. 1.

A. W-Type Slab Waveguide

In traditional slab waveguide with higher-index core squeezed by lower-index cladding layers, optical fields can be well guided inside the core region and exponentially decay outside. The propagation constant β is valued between the wavenumbers of the structure, i.e., $k_{clad} < \beta < k_{core}$, where k_{clad} and k_{core} are the wavenumbers of the cladding and the core, respectively. Under this restriction of physics, waves are not allowed to propagate laterally in the cladding layers, because their transverse propagation constant $\alpha = (k_{clad}^2 - \beta^2)^{1/2}$ is imaginary. Therefore, a simplest leaky-mode waveguide can be constructed by simply introducing a secondary (infinite) cladding region, outside the inner finite-thickness cladding layer, with structural wavenumber higher than β, forming the so-called W-type waveguide [9], [31], with its refractive-index profile shown in Fig. 2(a). This structure can, therefore, support

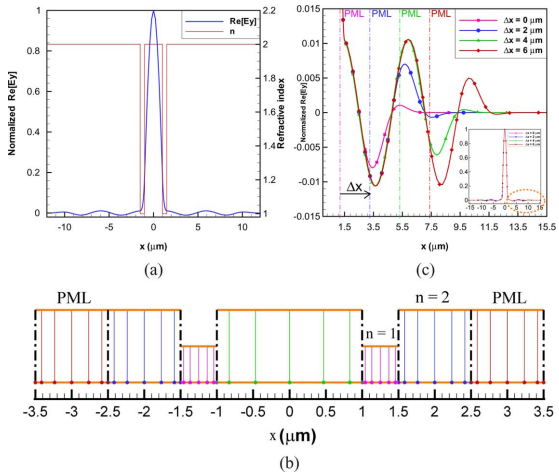

Fig. 2. (a) Structural refractive-index profile and Re[E_y] distribution showing leaky-wave characteristic for the W-type slab waveguide. (b) Domain partition (dashed lines for sub-domain edges) and LGL grid distributions (solid circles) for $N = 6$. (c) E_y field and leaky wave with the structural refractive index. (b) Absorption characteristics of Re[E_y] in the outer cladding layer for different distances, $\Delta x = 0, 2, 4$, and 6 μm, from PML to the inner cladding layer.

waves evanescently decaying in the inner cladding layer and sinusoidally propagating in the outer cladding layer. This behavior is similar to the tunneling effect of a finite-width energy barrier in quantum physics [8], [9].

The W-type waveguide of Fig. 2(a) is structured by 2-μm-thick core with refractive index $n = 2$ and 0.5-μm-thick inner cladding layer with $n = 1$. For supporting leaky waves, the material of the outer cladding layer is chosen to be the same as the core layer. This W-type leaky mode can be solved analytically [9], [31], and the obtained exact complex effective index of the fundamental transverse-electric (TE) mode on the given structure is $n_{eff} = 1.972708918684279 + j0.000003930939117$, when the operating wavelength is $\lambda = 1.5$ μm. Table I lists the PSFD computed complex effective indexes for different grid resolution or Ns, which apparently shows that the accuracy in n_{eff} reaches 10^{-15} as $N = 14$ is used. The sub-domain partitioning and unevenly distributed LGL mesh grids are illustrated in Fig. 2(b) for $N = 6$, where seven sub-domains are depicted including the PML ones. Only one PML sub-domain on each side is shown in Fig. 2(b) although each PML region has been actually composed of three sub-domains in the modeling. The loss of this W-type structure is about 143.02 dB/m, which can be further reduced by simply increasing the width of the inner cladding layer, where the fields exponentially decay.

Wave absorption in the PML region can be observed in Fig. 2(a), in which the Re[E_y] distribution is plotted. For better view of the magnitudes of the main field and the leaky field, we normalize the maximum field value in Fig. 2(a) to 1.0. The PML is placed in the regions $|x| \geq 7.5$ μm, where the absorption coefficient of the PML material is growing with increasing $|x|$. Transversely propagating leaky waves can be found in the outer cladding layers, and they become weaker as going deeper into the PML region, which will finally become zero as shown. To examine the effect of the PML position on the accuracy and the field profile, we take the W-type structure mentioned with $N = 14$ as an example and change the width

TABLE I
PSFD COMPUTED EFFECTIVE INDEXES FOR THE FUNDAMENTAL TE MODE OF THE M-TYPE SLAB WAVEGUIDE

N	Re[n_{eff}]	Im[n_{eff}]
4	1.959859883981541	0.000277972081040
6	1.972708918750655	0.000003930221217
8	1.972708918991630	0.000003930754473
10	1.972708918685354	0.000003930937988
12	1.972708918684282	0.000003930939124
14 (Δx = 6 μm)	1.972708918684277	0.000003930939117
14 (Δx = 4 μm)	1.972708918684279	0.000003930939116
14 (Δx = 2 μm)	1.972708918684279	0.000003930939117
14 (Δx = 0 μm)	1.972708918684279	0.000003930939118

of the outer cladding layer, that is, vary the distance Δx from PML to the inner cladding layer as shown in Fig. 2(c). Four distances, $\Delta x = 0, 2, 4$, and 6 μm, are tested, and the resultant Re[E_y] profiles in the outer cladding layer and PML region are shown in the figure. Note that the PML widths are fixed with 8 μm, and the vertical dashed lines indicate the start points of the PML region for different Δx's. The PSFD computed complex effective indexes of these four cases with $N = 14$ are listed in Table I and all of them are seen to be with accuracy on the order of 10^{-15}, which means that the position where the PML is placed has negligible effects on the computational accuracy.

B. M-Type Anti-Resonant Reflecting Optical Waveguide (ARROW)

In addition to guiding by the principle of total internal reflection (TIR), anti-resonance in a Fabry-Perot layer was also known to be capable of being utilized as wave-guiding mechanism [5]–[7]. It is well known that a layer of Fabry-Perot structure can be used as a cavity of wave transmission such that waves can be highly transmitted at resonance or reflected at anti-resonance. Taking advantage of high reflection at anti-resonance, two face-to-face Fabry-Perot layers operated under the anti-resonance condition can support wave-guiding in between, resulting in the so-called anti-resonant reflecting optical waveguide (ARROW). From the transmission spectrum of a Fabry-Perot layer, we know that portion of waves will penetrate the Fabry-Perot layers and outward propagate because the reflectivity R of each dielectric Fabry-Perot layer cannot reach 100%. Therefore, the ARROW is a leaky waveguide as well. Besides, since the Fabry-Perot layers have higher refractive index than the core and the outer cladding layers, as shown in Fig. 3, this ARROW can also be regarded as an M-type structure, compared to the W-type waveguide in Fig. 2(a).

Two proposed ARROW structures are analyzed here to examine the ability and accuracy of the PSFD method treating such kind of leaky-mode waveguide with multiple interference mechanism. The first M-type structure, case-A, is the one considered in [5]. The core and the outer cladding layers are made of SiO_2 with $n = 1.46$, and the Fabry-Perot layers are made of TiO_2 with higher index $n = 2.3$. The operating wavelength is $\lambda = 0.6328$ μm, and the waveguide widths of the core and the Fabry-Perot layers are 4 μm and 0.089 μm, respectively.

TABLE II
PSFD COMPUTED EFFECTIVE INDEXES FOR THE FUNDAMENTAL TE MODE OF THE M-TYPE SLAB WAVEGUIDE

N	Re[n_{eff}] (Case-A)	Im[n_{eff}] (Case-A)	Re[n_{eff}] (Case-B)	Im[n_{eff}] (Case-B)
4	1.457855466583192	0.000005587298538	0.9978547439568767	0.000013218898690
6	1.45785585136149	0.000005398702142	0.9978604800321252	0.000014578997356
8	1.457855851231652	0.000005400603918	0.9978605202336727	0.000014581325891
10	1.457855851273043	0.000005400595700	0.9978605202602324	0.000014581278856
12	1.457855851272849	0.000005400596676	0.9978605202596181	0.000014581278387
14	1.457855851272856	0.000005400596683	0.9978605202596357	0.000014581278392
16	1.457855851272856	0.000005400596683	0.9978605202596358	0.000014581278392

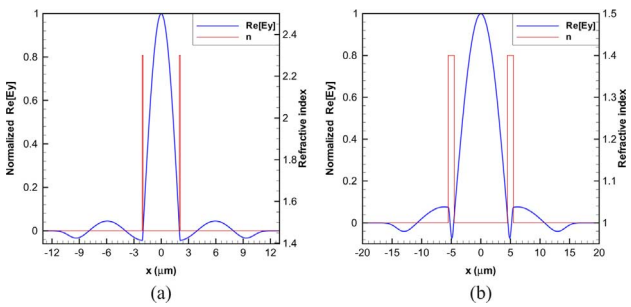

Fig. 3. Structural refractive-index profiles and Re[E_y] profiles showing leaky-wave characteristic for the M-type slab waveguide. (a) case-A. (b) case-B.

The second structure, case-B, was proposed in [6], which is an air-core pipe waveguide. Here we consider its 1-D slab structure version first, and the circular structure will be discussed in Subsection IV.E., which has $n = 1.0$ for the core and the outer cladding layers, and $n = 1.4$ for the Fabry-Perot layers. The widths for the core and the Fabry-Perot layer are 9 μm and 1 μm, respectively, and the operating wavelength is $\lambda = 1.2$ μm.

The PSFD calculated complex effective indexes for the fundamental TE mode for both cases are shown in Table II for different Ns. The leaky modes on this M-type waveguide can also be solved analytically [9], [31], and the obtained exact complex effective indexes for the case-A and case-B structures are $n_{eff} = 1.457855851272856 + j0.0000054005966836$ and $0.997860520259636 + j0.000014581278392$, respectively. Apparently, the PSFD accuracy reaches the order of 10^{-15} for both cases. The Re[E_y] profiles for case-A and case-B are shown in Fig. 3(a) and (b), respectively, along with their refractive-index profiles. The modal fields are seen to be mainly distributed between the two Fabry-Perot layers, with those in the outer claddings laterally propagating to both ends. In case-A, the PML regions are defined to be $|x| \geq 8.089$ μm, within which the propagating waves gradually decay to zero as shown in Fig. 3(a). Similarly, the PML regions for case-B are taken to be $|x| \geq 11.5$ μm, and the laterally going waves are seen to be well absorbed in Fig. 3(b). Notice that the maximum of Re[E_y] is normalized to 1.0 in both figures.

C. Circular Fiber Waveguide

We have shown above that the PSFD method with stretched coordinate PML can accurately solve 1-D leaky waveguide modes with the mechanism of total internal reflection or anti-resonance. We shall then discuss the application of this PSFD method to solve 2-D waveguides. Before studying leaky

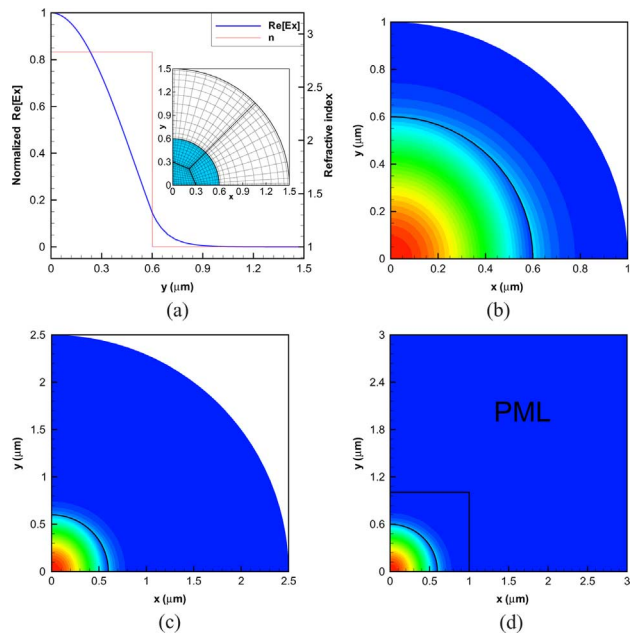

Fig. 4. Electric-field distributions of the HE_{11} mode of the circular fiber waveguide. (a) Re[E_x] profile along the y-axis, structural refractive-index profile, and in the inset sub-domain division and grid mesh. (b) $|E_x|$ profile for the case with 0.4-μm-radius cladding layer. (c) $|E_x|$ profile for the case with 1.9-μm-radius cladding layer. (d) $|E_x|$ profile for the case with 0.4-μm-cladding layer and PML.

waveguides, the accuracy of the PSFD analysis of 2-D structures and the effect of PML will be examined first. Circular fiber is a suitable example for examination, and an air-cladded fiber with core radius of 0.6 μm and $n = \sqrt{8}$ is considered. Because of its structural symmetry, we can analyze just one quarter of the whole structure for acceleration of computation, as shown in the inset of Fig. 4(a), with perfect electric conductor (PEC) or perfect magnetic conductor (PMC) placed at the left and bottom edges, respectively. The inset shows the mesh division using $N = 12$ and the one-quarter computational domain is partitioned into curvilinear sub-domains, with the shape of the material interface being well fitted with the boundaries of corresponding sub-domains. For this fiber, the analytical effective index for the fundamental HE_{11} mode is $n_{eff} = 2.684019321609156$ when the operating wavelength is $\lambda = 1.5$ μm [1].

Three structures are examined. The first one has an air cladding layer of 0.4-μm thickness as shown in Fig. 4(b), the second one has air cladding layer of 1.9-μm thickness as depicted in Fig. 4(c), and the third one is similar to the first

TABLE III
PSFD COMPUTED EFFECTIVE INDEXES FOR THE HE_{11} MODE OF THE CIRCULAR FIBER (THE ANALYTICAL $n_{eff} = 2.684019321609156$)

N	n_{eff} (0.4-μm cladding)	n_{eff} (1.9-μm cladding)	Re[n_{eff}] (with PML)	Im[n_{eff}] (with PML)
4	2.684028578565857	2.684817661481339	2.684165820553023	0.000000003635876
6	2.684013318320761	2.684034764094687	2.684021278395971	0.000000000357849
8	2.684013297283687	2.684019429341273	2.684019331653940	0.000000000004183
10	2.684013297272886	2.684019322034613	2.684019321645284	0.000000000000089
12	2.684013297272882	2.684019321610760	2.684019321609498	0.000000000000002
14	2.684013297272882	2.684019321609156	2.684019321609159	0.000000000000001

one but with PML layers added as shown in Fig. 4(d). Note that PEC boundary condition is placed at the outermost edge of the cladding layer, where mode fields are supposed to decay to almost zero there. The PSFD calculated effective indexes with N varied from 4 to 14 are shown in Table III for these three structures. Apparently, the first case with air cladding layer of 0.4-μm thickness is seem to have only 10^{-6} accuracy, but the second case with air cladding layer of 1.9-μm thickness has 10^{-15} accuracy, instead. This is because the fields exponentially decay in the cladding layer, but not quite close to zero at the outer PEC for the first case since the cladding layer is not thick enough. For the third structure, which is designed with additional PML layers added outside the air cladding of the first case, the accuracy of the PSFD computed effective index is achieved, again, on the order of 10^{-15} when $N = 14$. This result reveals that although the PML is placed close to the core-cladding interface with the mode fields not yet decaying to zero at $x = y = 1$ μm, such PML arrangement is found to have negligible effects on the calculation accuracy, just like those tests done for the 1-D W-type waveguide in Fig. 2(b). Notice that the imaginary parts of n_{eff} in the third case in Table III come from the introduction of PML. These non-zero values are not physically meaningful since they are comparatively much smaller than the values of the real parts and can be considered as computation noises. They actually become almost zero as N is large enough, as seen in Table III.

The $|E_x|$ profiles are shown in Fig. 4(b), (c), and (d) for the three cases, and the Re[E_x] versus y curve of Fig. 4(c) is shown in Fig. 4(a) along with the structural refractive-index profile. Here we show the 1-D E_x field along the y-axis, because it maintains tangential continuity across different materials. The field profiles, in the format of either the absolute value or the real part, shown in the following are all normalized to 1.0, and the profiles of Fig. 4(b), (c), and (d) should be indistinguishable since the field solution differences among them are on the order of 10^{-6}.

D. W-Type Circular Waveguide

The first 2-D leaky-mode waveguide to be discussed here is, again, the simplest W-type structure, which has the same guiding mechanism as the 1-D ones. This 2-D W-type waveguide has a circularly symmetric index profile with its radially dependent profile the same as the profile of the 1-D W-type structure in Fig. 2(a), as shown in Fig. 5(a). That is, the core has a radius of 1 μm and $n = 2.0$, and the lower-index inner cladding layer has 0.5-μm thickness with $n = 1.0$, and the outer cladding layer is of the same material as the core for supporting wave

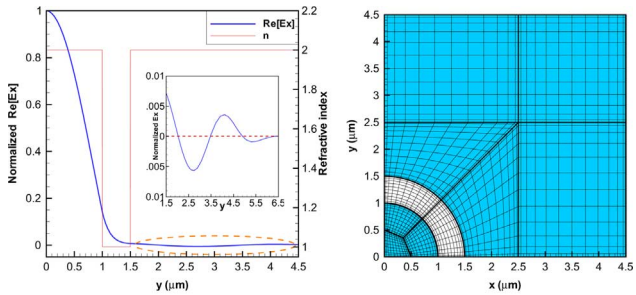

Fig. 5. (a) Structural refractive-index profile and Re[E_x] of the HE_{11} mode versus y distribution for the W-type circular waveguide with the enlarged Re[E_x] profile for $1.5\ \mu\text{m} < y < 6.5\ \mu$m in the inset showing the leaky-wave characteristic. (b) Sub-domain arrangement and grid mesh in the computational region.

TABLE IV
PSFD COMPUTED EFFECTIVE INDEXES FOR THE HE_{11} MODE OF THE W-TYPE CIRCULAR WAVEGUIDE

N	Re[n_{eff}]	Im[n_{eff}]
4	1.927955256717321	0.000010232110091
6	1.927952220566292	0.000009664157400
8	1.927952222316175	0.000009664102005
10	1.927952222319007	0.000009664102159
12	1.927952222319014	0.000009664102146
14	1.927952222319016	0.000009664102145

leakage. The sub-domain division in one quarter of the structural cross-section is illustrated in Fig. 5(b) for $N = 12$. The absorptive PML region is set at $x \geq 2.5$ μm and $y \geq 2.5$ μm, occupying the three rectangular sub-domains in Fig. 5(b). The PSFD computed complex effective indexes for the fundamental HE_{11} mode for different Ns are listed in Table IV, which shows 10^{-15} self-converged accuracy as well. The obtained loss is about 351.6 dB/m, which is larger than that of the 1-D structure and can be reduced by increasing the width of the inner cladding layer.

The Re[E_x] profile along the y-axis is depicted in Fig. 5(a), which shows wave-guiding in the core region, exponentially decaying in the inner cladding layer, sinusoidally propagating in the outer cladding layer, and being absorbed in the PML region. The leaky waves can be seen to be well absorbed in the PML region in the expanded plot shown in the inset of Fig. 5(a). We have found that the position of the PML region has negligible effect on the numerical accuracy. The PSFD computed electric and magnetic mode-field distributions are shown in Fig. 6(a)–(f). It shows that the $|E_x|$ and $|H_y|$ profiles are similar, and so are the $|E_y|$ and $|H_x|$ profiles, while the $|E_z|$

TABLE V
PSFD COMPUTED EFFECTIVE INDEXES FOR THE HE_{11} MODE OF THE M-TYPE FIBER WAVEGUIDE

N	Re[n_{eff}] (Case-A)	Im[n_{eff}] (Case-A)	Re[n_{eff}] (Case-B)	Im[n_{eff}] (Case-B)
4	1.454972011590725	0.000067964021055	0.995046857892952	0.000107811869149
6	1.454972795382911	0.000067384270784	0.995074543892952	0.000119190084682
8	1.454972795546622	0.000067382511442	0.995074815513635	0.000119172594021
10	1.454972795544452	0.000067382509617	0.995074815411661	0.000119172090879
12	1.454972795544450	0.000067382509619	0.995074815411650	0.000119172090790
14	1.454972795544450	0.000067382509619	0.995074815411650	0.000119172090790

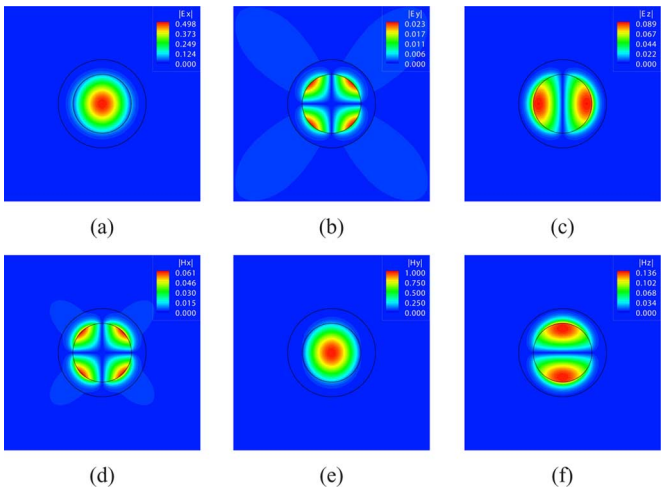

Fig. 6. Field profiles of the HE_{11} mode of the W-type fiber waveguide. (a) $|E_x|$. (b) $|E_y|$. (c) $|E_z|$. (d) $|H_x|$. (e) $|H_y|$. (f) $|H_z|$.

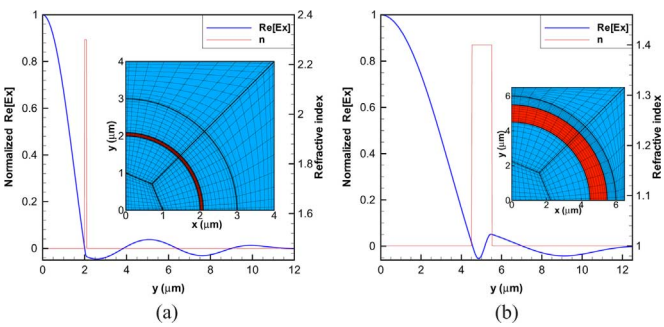

Fig. 7. Structural refractive-index profile and Re[E_x] of the HE_{11} mode versus y distribution for the M-type circular waveguide with the inset showing the sub-domain arrangement and the grid mesh. (a) case-A. (b) case-B.

and $|H_z|$ profiles have rotated similarity. Comparing with the standard fiber waveguide, the field patterns are almost similar, except the W-type fiber possesses leaky waves in the outer cladding layer.

E. M-Type Circular Waveguide (ARROW Structure)

As in the 1-D case, the 2-D M-type waveguide is an ARROW structure. Again, we consider two circularly symmetric index profiles with their radially dependent profiles the same as those of the 1-D ARROWs plotted in Fig. 3(a) (case-A) and (b) (case-B), respectively, as shown in Fig. 7(a) and (b). In the case-A structure, both the core and the outer cladding are with $n = 1.46$, the core radius is 2 μm, and the Fabry-Perot layer is with $n = 2.3$ and 0.089-μm thickness. The case-B structure is a pipe waveguide studied in [6] with the following parameters: core radius of 9 μm, Fabry-Perot layer of thickness 1 μm and $n = 1.4$, and the core and the cladding are simply air. The field confinement and leakage property of the 2-D ARROW depends critically on the operating wavelength due to the Fabry-Perot resonant condition. Take case-B as an example, the relationship between the attenuation constant and the operating frequency can be seen in [6], which correlates with the Fabry-Perot wave transmission/reflection spectrum. Here, we choose $\lambda = 1.2$ μm at which a Fabry-Perot-layer transmission minimum or an anti-resonance occurs, resulting in better field confinement in the waveguide.

The computational sub-domain partitioning and grid meshes for both cases are shown in the insets of Fig. 7(a) and (b), respectively. The PMLs, not shown in the insets, are located in the region ($x \geq 6$ μm and $y \geq 6$ μm) for the case-A structure in Fig. 7(a) and in the region ($x \geq 6.5$ μm and $y \geq 6.5$ μm) for the case-B structure in Fig. 7(b). The PSFD computed complex refractive indexes for the fundamental HE_{11} mode for both structures are listed in Table V for different Ns, which shows self-convergence of accuracy on the order of 10^{-15} in both ones. To examine the wave leakage and PML absorption, we plot in Figs. 7(a) and (b) the respective Re[E_x] profiles along the y-axis. Apparently, the leaky waves can be well absorbed in both cases since it is seen the fields decrease gradually in the PML region and approach zero at the edge of the computational domain.

The PSFD computed electric and magnetic mode-field distributions are shown in Fig. 8(a)–(f) for case-A and in Fig. 9(a)–(f) for case-B, respectively, for comparison. From Table V, we see that Im[n_{eff}] for case-B at the considered wavelength is larger than that for case-A, as can be understood from the field distributions in Figs. 8 and 9. The loss of case-B can become smaller if it is operated at other dips in the higher frequency range [6]. The case-B structure has the advantage of avoiding material loss in the core since the guiding core is simply an air region in addition to its simple pipe geometry which can make the manufacturing very easy.

F. Microstructured Six-Air-Hole Fiber Waveguide

So far, we have examined the accuracy of the PSFD method with the PML by analyzing several standard 1-D and 2-D W-type and M-type leaky waveguides, and the resultant accuracy has been demonstrated to be on the order of 10^{-15} for all cases. Now, we will apply this PSFD method to solve waveguides with more complicated structures.

First, we consider the popularly studied microstructured six-air-hole fiber [17]–[19], [21], as shown in Fig. 1(d). With the

TABLE VI
PSFD COMPUTED EFFECTIVE INDEXES FOR THE FUNDAMENTAL MODE OF THE SIX-AIR-HOLE WAVEGUIDE FOR THE $p = 1$ AND $p = 3$ MODES

N	Re[n_{eff}] ($p = 1$)	Im[n_{eff}] ($p = 1$)	Re[n_{eff}] ($p = 3$)	Im[n_{eff}] ($p = 3$)
4	1.438367658633584	0.000001321295554	1.445395882102650	0.000000042017309
6	1.438364943632872	0.000001432990316	1.445395236589104	0.000000031910666
8	1.438364934410756	0.000001416728792	1.445395232274384	0.000000031944327
10	1.438364934183757	0.000001416477217	1.445395232151004	0.000000031945254
12	1.438364934178938	0.000001416475936	1.445395232149312	0.000000031945250
14	1.438364934178881	0.000001416475992	1.445395232149294	0.000000031945250
16	1.438364934178884	0.000001416475997	1.445395232149295	0.000000031945250

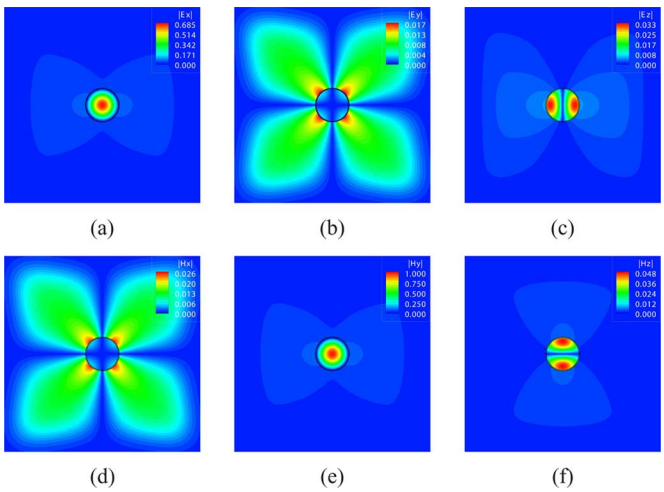

Fig. 8. Field profiles of the HE_{11} mode of the case-A M-type fiber waveguide. (a) $|E_x|$. (b) $|E_y|$. (c) $|E_z|$. (d) $|H_x|$. (e) $|H_y|$. (f) $|H_z|$.

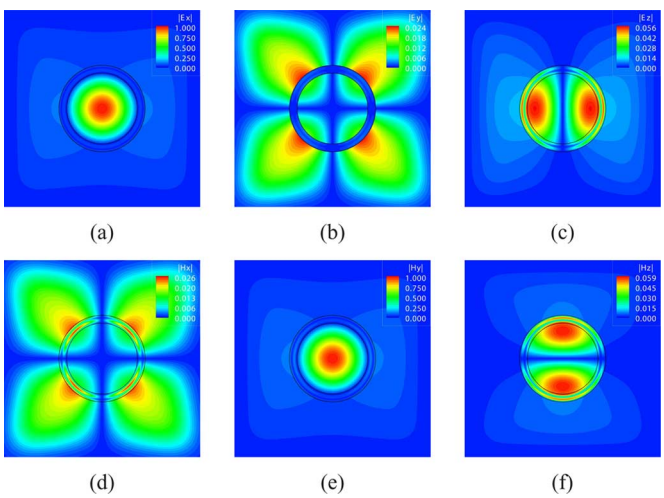

Fig. 9. Field profiles of the HE_{11} mode of the case-B M-type fiber waveguide. (a) $|E_x|$. (b) $|E_y|$. (c) $|E_z|$. (d) $|H_x|$. (e) $|H_y|$. (f) $|H_z|$.

structural symmetry, we can again treat only one quarter of the waveguide cross-section, as we have done in the previous three circular waveguide structures. According to [17]–[19], and [21], six holes are hexagonally arranged, and the hole pitch, i.e., the center-to-center distance of adjacent holes, is $\Lambda = 6.75$ μm. The radius of each hole is $R = 2.5$ μm, and the refractive indexes for the fiber and the hole are $n = 1.45$ and 1.0, respectively. With the cladding extended to infinity, this structure possesses a similar characteristic as the W-type fiber since the six air-holes create an equivalent lower-index ring structure,

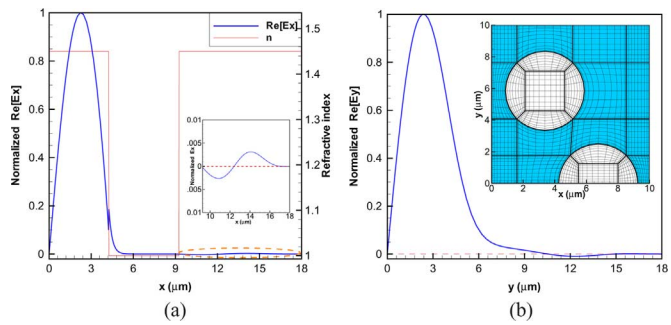

Fig. 10. (a) Structural refractive-index profile along the y-axis and Re[E_x] of the fundamental mode versus x distribution for the six-air-hole waveguide with the enlarged Re[E_x] profile for 9 μm $< x <$ 18 μm in the inset showing the leaky-wave characteristic. (b) Re[E_y] versus y distribution with the inset showing the sub-domain arrangement and grid mesh.

making the structure to support leaky modes with complex effective indexes.

The $p = 1$ and $p = 3$ modes, as defined in [17] and [18], are considered here at $\lambda = 1.45$ μm. The PSFD computed complex effective indexes for these two modes are listed in Table VI for different Ns. Accuracy of self-convergence on the order of 10^{-14} is observed for this complicated structure. According to the result of the multipole method proposed in [18], the computed effective index for this $p = 1$ mode was $n_{eff} = 1.43836493424529 + j0.00000141647574$, which agrees well with our results to 10^{-9} for the real part and to 10^{-12} for the imaginary part. On the other hand, as mentioned in the Introduction, a new high-order boundary-integral-equation (BIE) method was reported recently and shown to achieve exponential convergence and extremely high accuracy [19]. The computed effective index for the $p = 3$ mode provided in [19] is $n_{eff} = 1.4453952321493 + j0.000000003194529$, which agrees with our results to the order of 10^{-13} for both the real and imaginary parts.

To observe the leaky waves and their attenuations in the PML layer, Re[E_x] versus x and Re[E_y] versus y profiles are shown in Fig. 10(a) and (b), respectively. Since scanning of E_x along the x-axis will pass through the air-hole, discontinuity of Re[E_x] would occur, as can be seen in Fig. 10(a). Domain partitioning and grid meshes in the computation are shown in the inset of Fig. 10(b). Again, one quarter the waveguide cross-section is treated and the PML, not shown in Fig. 10(b), is designed to be in the region ($x \geq 10$ μm and $y \geq 10$ μm). From the inset in Fig. 10(a), the field can be seen well absorbed in the PML region and approaching zero eventually.

The PSFD computed electric and magnetic mode-field distributions are shown in Fig. 11(a)–(f) for the $p = 1$ mode and in

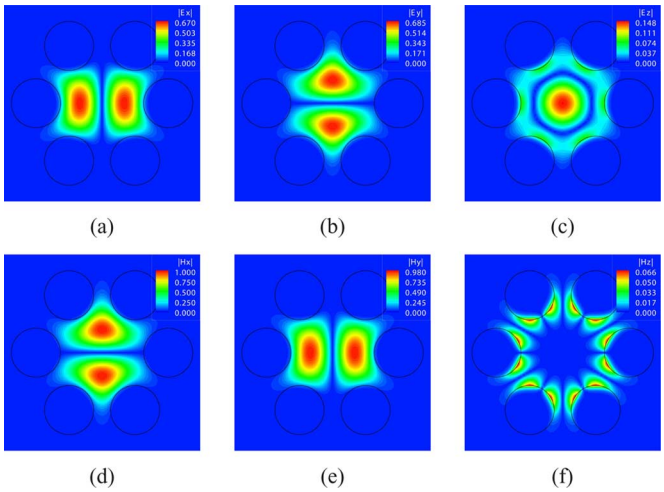

Fig. 11. Field profiles of the $p = 1$ mode of the six-air-hole fiber waveguide. (a) $|E_x|$. (b) $|E_y|$. (c) $|E_z|$. (d) $|H_x|$. (e) $|H_y|$. (f) $|H_z|$.

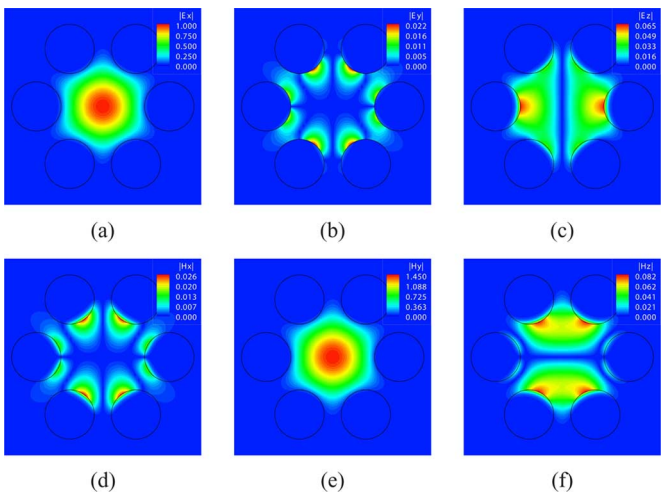

Fig. 12. Field profiles of the $p = 3$ mode of the six-air-hole fiber waveguide. (a) $|E_x|$. (b) $|E_y|$. (c) $|E_z|$. (d) $|H_x|$. (e) $|H_y|$. (f) $|H_z|$.

Fig. 12(a)–(f) for the $p = 3$ mode, which are similar to those presented in [17] and [21]. Similar to the standard circular fibers, the $|E_x|$ and $|H_y|$ profiles are alike, and so are the $|E_y|$ and $|H_x|$ profiles.

Up to now we have analyzed four kinds of 2-D waveguides with round material interfaces, and the PSFD computed effective indexes are listed in Tables III, IV, V, and VI, respectively. Based on the data in the tables, as a useful summary, we calculate and plot the errors of n_{eff} versus N in Fig. 13(a)–(d) to show the respective characteristics of numerical convergence of the developed PSFD mode solver. For each N, the error of n_{eff} is defined as the absolute value of the difference between the calculated n_{eff} and an accurate reference n_{eff}. Fig. 13 is presented in logarithmic scales, and exponential convergence of computational accuracy is observed in all four cases, which means that numerical errors can be fast reduced by a relatively small increase in the number of grid points. Note that the calculated errors in Fig. 13(a) are based on the data assuming the air cladding layer is of 1.9 μm thickness and the reference n_{eff} being the analytical solution, while the reference n_{eff}s for Fig. 13(b)–(d) are respectively those n_{eff}s corresponding

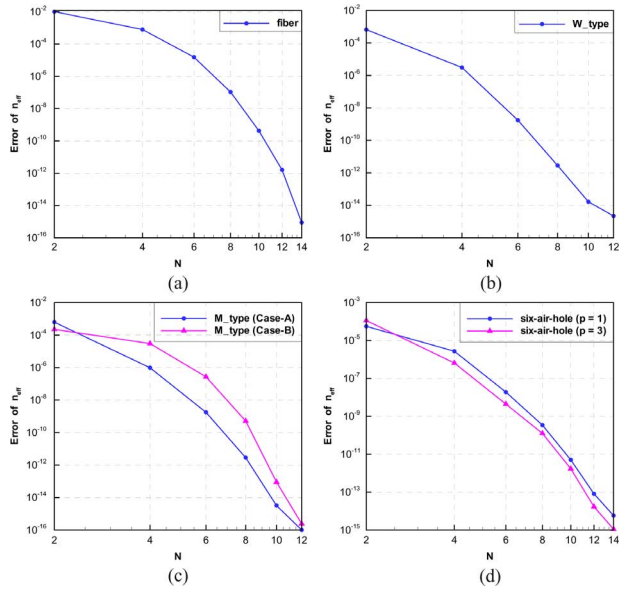

Fig. 13. Exponential convergence characteristics of the error of n_{eff} versus N. (a) The circular fiber. (b) The W-type circular fiber. (c) The M-type circular fiber. (d) The six-air-hole fiber waveguide.

to the respective maximum N value in Tables IV, V, and VI. Regarding computer resources used, we provide the following data for the case of the circular fiber obtained using one core on a 2.66-GHz Intel® Core™ i7-920 PC machine. With $N = 4$, 6, 8, 10, 12, and 14, the corresponding computation times are 4.14 s, 20.4 s, 68.11 s, 212.38 s, 443.58 s, and 783.13 s, respectively, the matrix sizes are 1050, 2058, 3402, 5082, 7098, and 9450, respectively, and the memories taken are 1864 kB, 2112 kB, 2356 kB, 2676 kB, 3120 kB, and 3588 kB, respectively. It can be seen our program uses small memories. Fig. 13(a) reveals that with $N = 8$ the error of n_{eff} already goes down to the practically impressive order of 10^{-7}.

G. RIB Waveguide

We have analyzed several leaky-mode waveguides with circular interfaces, and the PSFD method is shown to give 10^{-15} accuracy through self-convergence tests. It has been shown in [24] that using the PSFD method for analyzing (nonleaky) dielectric channel waveguides with sharp dielectric corners can provide only 10^{-8} accuracy in the effective index with $N = 10$; with $N = 16, 24,$ and 40, the accuracy improves to 10^{-9}, 10^{-10}, and 10^{-11}, respectively. The convergence characteristic is not an exponential one as in the 2-D waveguides without corners discussed so far but more with a first-order convergent rate. This is due to that the sharp dielectric corners are associated with electric-field singular points, which ruins the computation [24].

Below, we will consider two rectilineal waveguides, the rib waveguide and the photonic wire waveguide, as shown in Fig. 1(e) and (f), respectively. First, in this subsection, the rib waveguide is examined. The waveguide structure is the same as that studied in [29]. Referring to Fig. 1(e), the thicknesses in the rib region are $H = 1.0$ μm and $h = 0.5$ μm, the rib width is $W = 3.0$ μm, and $n = 1.0$ (air), 3.44, and 3.4 for the upper cladding, the core, and the substrate, respectively. The operating wavelength is $\lambda = 1.15$ μm. The fundamental

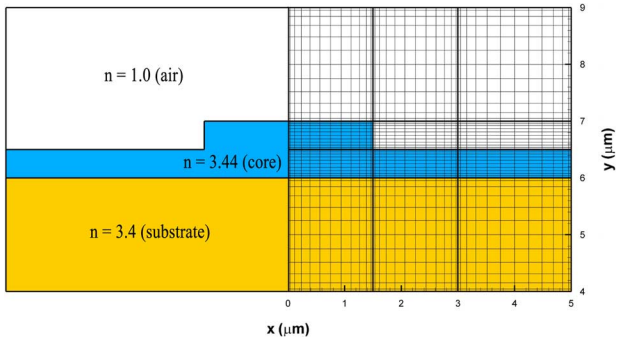

Fig. 14. Sub-domain arrangement and grid mesh for the rib waveguide.

TABLE VII
PSFD COMPUTED EFFECTIVE INDEXES FOR THE FUNDAMENTAL TE MODE OF THE RIB WAVEGUIDE

N	n_{eff}
4	3.414329827640850
6	3.413414917379402
8	3.413183007067949
10	3.413138730115563
12	3.413132756729537
14	3.413132183989132
16	3.413132136900558
20	3.413132130779760
24	3.413132132794152
28	3.413132135245575
32	3.413132137218818

TE guided mode of this rib waveguide is not a leaky one, but it is a good case for examining the effect of the sharp corners in a more complicated waveguide structure than the simple channel waveguide, since it has long been an example for benchmarking waveguide mode solvers including in [32]. And such examination would be useful before studying the photonic wire waveguide in the next subsection. Fig. 14 shows the rib waveguide structure and the designed sub-domain arrangement for half structure due to symmetry. PML regions (not shown) are put outside the right, bottom, and top sides with thicknesses 6 μm (three sub-domain layers), 4 μm (two sub-domain layers), and 2 μm (one sub-domain layer), respectively. The PSFD computed effective indexes for different Ns are listed in Table VII, and the finite-difference method obtained value of $n_{eff} = 3.413132 \pm 3 \times 10^{-6}$ provided in [32] is used for comparison. Apparently, the PSFD calculation reaches 3.413132 when $N = 12$, and then the convergent rate slows down. However, with larger N used, as seen in Table VII for N from 16 to 32, better accuracy can be obtained, and we can achieve two more accuracy digits than that in [32], i.e., $n_{eff} = 3.41313214$ (after rounding) with self-convergent accuracy on the order 10^{-8}.

The calculated $|E_x|$, $|E_y|$, $|E_z|$, $|H_x|$, $|H_y|$, and $|H_z|$ profiles for the fundamental TE mode are shown in Fig. 15(a)–(f), respectively. The mode fields are well guided in the thicker portion of the rib region, and field singular points can be seen in Fig. 15(b).

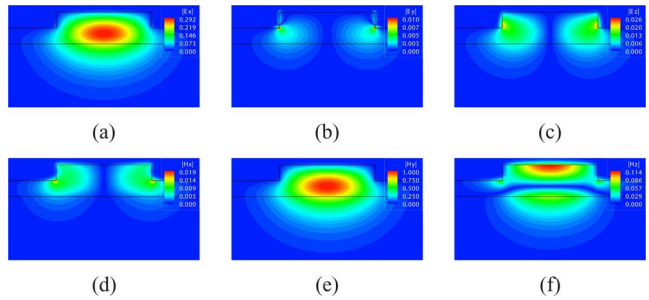

Fig. 15. Field profiles of the fundamental TE mode of the rib waveguide. (a) $|E_x|$. (b) $|E_y|$. (c) $|E_z|$. (d) $|H_x|$. (e) $|H_y|$. (f) $|H_z|$.

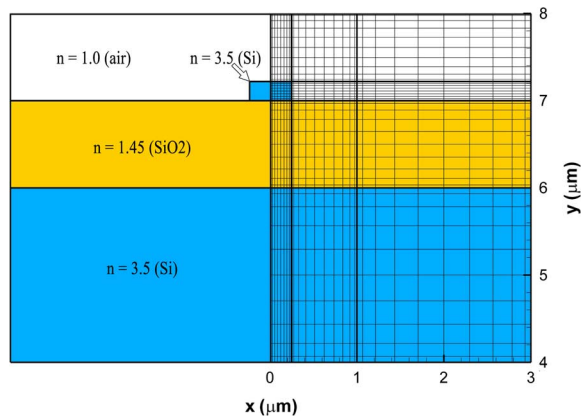

Fig. 16. Sub-domain arrangement and grid mesh for the photonic wire waveguide.

H. Photonic Wire Waveguide

The photonic wire waveguide or photonic wire has been an essential structure in recently developed high-density photonic integrated circuits, and the computed effective indexes of its fundamental mode have been compared among ten different numerical methods or solvers in [30]. As shown in Fig. 16, the guiding core and the substrate are both made of silicon with $n = 3.5$ and there is a SiO_2 buffer layer between them with $n = 1.45$. The upper cover medium is air, resulting in a high-index-contrast structure. The rectangular core has of course sharp corners. One important characteristic is that the limited thickness of the SiO_2 buffer causes the fundamental mode to leak power into the substrate, and the accurate determination of Im$[n_{eff}]$ becomes a main concern. To compare with the results in [30], we adopt the same parameters: the width and the height of the core being 0.5 μm and 0.22 μm, respectively, the thickness of the buffer layer being 1.0 μm, and $\lambda = 1.55$ μm. The designed sub-domain arrangement for half structure is also shown in Fig. 16. Again, PML regions (not shown) are put outside the right, bottom, and top sides with thicknesses 4 μm (three sub-domain layers), 4 μm (two sub-domain layers), and 2 μm (one sub-domain layer), respectively. The PSFD computed complex effective indexes for different Ns are listed in Table VIII, and with N up to 32. From the convergence trend, we would have confidence that Re$[n_{eff}] = 2.41237$ (order of 10^{-5} accuracy) and Im$[n_{eff}]$ falls betweem 2.91×10^{-8} and 2.92×10^{-8}, showing slow convergent rate for this high-index-contrast structure with corners compared with all cases discussed above.

The calculated effective indexes by ten different methods or solvers, as given in Table VI of [30], are similarly listed in

TABLE VIII
PSFD COMPUTED EFFECTIVE INDEXES FOR THE FUNDAMENTAL MODE OF THE PHOTONIC WIRE WAVEGUIDE

N	Re[n_{eff}]	Im[n_{eff}]
4	2.390482909644422	2.2502459×10^{-8}
6	2.412928964014647	3.0647138×10^{-8}
8	2.412454190888035	4.9832197×10^{-8}
10	2.412413768252360	3.5744559×10^{-8}
12	2.412398013885063	2.3180120×10^{-8}
14	2.412389601631874	4.5563542×10^{-8}
16	2.412384521810727	3.1565139×10^{-8}
20	2.412379043823438	3.0185470×10^{-8}
24	2.412376369646066	2.9509228×10^{-8}
28	2.412374903200264	2.9279178×10^{-8}
32	2.412374029676081	2.9198372×10^{-8}

TABLE IX
COMPUTED EFFECTIVE INDEXES FOR THE FUNDAMENTAL MODE OF THE PHOTONIC WIRE WAVEGUIDE FROM TEN METHODS AS LISTED IN TABLE VI OF [30] AND FROM THE PSFD METHOD

Method	Re[n_{eff}]	Im[n_{eff}]
Effective index	2.45	2.4×10^{-3}
Perturbation	2.35	3.0×10^{-7}
BPM Obayya	2.413340	2.7×10^{-8}
FEM Uranus	2.4131	2.97×10^{-8}
FEM Parma	2.41233	2.45×10^{-8}
Olympios	2.413	2.9×10^{-8}
FimmWave	2.41235	2.688×10^{-8}
CAMFR	2.412372	2.9135×10^{-8}
Aperiodic Fourier modal	2.412372	2.91348×10^{-8}
Plane wave admittance	2.4126	2.910×10^{-8}
PSFD (this work)	2.412374	2.9198×10^{-8}

Table IX together with our PSFD result using $N = 32$ for comparison. It was concluded in [30] that for Re[n_{eff}], four solvers agree on five significant digits 2.4123 with CAMFR and aperiodic fourier modal method even agreeing up to seven significant digits, and for Im[n_{eff}], three solvers agree on three significant digits 2.91×10^{-8} with CAMFR and aperiodic fourier modal method again agreeing on five significant digits after rounding. It is seen that our PSFD result agrees with CAMFR and aperiodic fourier modal method on six significant digits for Re[n_{eff}] (2.41237) and with a deviation less than 0.01×10^{-8} for Im[n_{eff}] (2.92×10^{-8} after rounding). As mentioned in the first paragraph of the previous subsection for rib waveguide, the sharp dielectric corners are with electric-field singular points and ruin the spectral convergence [24]. Therefore, although Table III shows the possible decreasing trend for the values of both Re[n_{eff}] and Im[n_{eff}], such decrease would be slow with N. We did not pursue further computation since the $N = 32$ one has already been expensive.

Fig. 17 shows the Re[E_x] profile along the y-axis at $x = 0$ together with the waveguide refractive-index profile. The mode field is seen mostly guided in the core, decaying in the SiO_2 buffer layer, leaking into the Si substrate, and absorbed by the PML layer. The PML is placed at $y < 4$ μm (substrate) and the enlarged field profile depicted in the inset of Fig. 17 clearly shows the leaky behavior and the well-absorption by the PML.

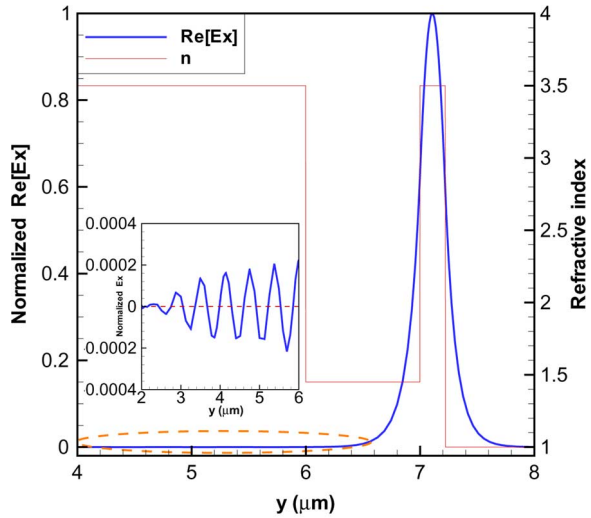

(a)

Fig. 17. Structural refractive-index profile along the y-axis at $x = 0$ and Re[E_x] of the fundamental mode versus y distribution at $x = 0$ for the photonic wire waveguide with the enlarged Re[E_x] profile for $2\mu\text{m} < x < 6$ μm in the inset showing the leaky-wave characteristic.

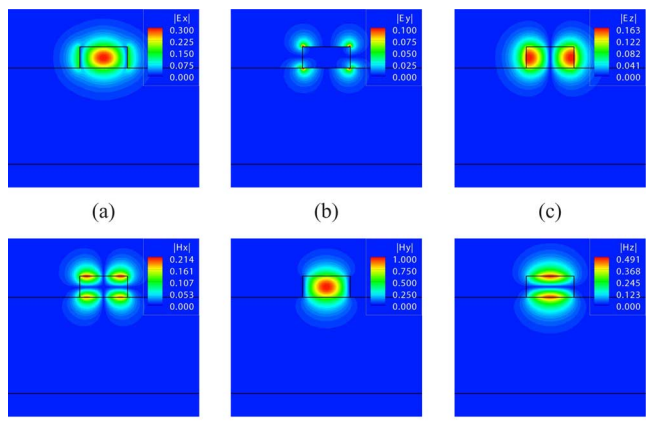

Fig. 18. Field profiles of the fundamental mode of the photonic wire waveguide. (a) $|E_x|$. (b) $|E_y|$. (c) $|E_z|$. (d) $|H_x|$. (e) $|H_y|$. (f) $|H_z|$.

The PSFD calculated $|E_x|$, $|E_y|$, $|E_z|$, $|H_x|$, $|H_y|$, and $|H_z|$ profiles for the fundamental mode are shown in Fig. 18(a)–(f), respectively. The field singular points can be seen in Fig. 18(b).

V. CONCLUDING REMARKS

We have incorporated the stretched coordinate PMLs into the recently developed pseudospectral frequency-domain (PSFD) method waveguide mode solver which employs a penalty scheme [24] so that leaky modes can be determined with high-accuracy complex effective indexes. Applications of the new PSFD solver to several standard leaky-mode slab and circular waveguides, including the W-type and M-type ones, demonstrate that computational accuracy for the effective indexes of their fundamental modes can be on the order of 10^{-15}. For the popularly studied more complicated microstructured six-air-hole fiber, our PSFD solver can achieve self convergence of accuracy in the effective index on the order of 10^{-14}, and the comparison with a new high-order boundary-integral-equation (BIE) method reported recently [19] shows that

the agreement between the two solvers is up to the order of 10^{-13} for both the real and imaginary parts of the computed effective index for the $p = 3$ mode. As for rectilineal waveguides with sharp corners, PSFD analyses of the rib waveguide and the photonic wire have been conducted. As investigated in [24], sharp dielectric corners are associated with electric-field singular points and ruin the exponential-convergence characteristic of the PSFD computation. Nevertheless, compared with the prior high-accuracy finite-difference analysis of the rib waveguide in [32], we can achieve two more accuracy digits, with self-convergent accuracy on the order 10^{-8}, for the computed effective index of the fundamental TE mode. For the high-index-contrast photonic wire with substrate leakage, the PSFD solver provides an effective index for the fundamental mode close to the possible best results offered by CAMFR and aperiodic fourier modal method among ten methods compared in [30] with the agreement on six significant digits for the real part and on three digits for the imaginary part.

Some remarks regarding the advantages of this proposed PSFD method waveguide mode solver are addressed below. Solving second-order Helmholtz equations in terms of the two transverse-magnetic field components has been a popular approach in full-vectorial waveguide analysis. The PSFD formulation of [21] was based on such approach with PMLs implemented. The present PSFD formulation is constructed using first-order differential equations written from Maxwell's equations and the six field components are included. Obviously, under the same sub-domain arrangement, the number of unknowns becomes larger, which could be the major disadvantage. In [24], on which the present formualtion is based, the possibility of reducing the total number of discrete equations as well as the field components included to reduce the computational work has been discussed in its concluding remarks, where it was also pointed out that one advantage of the first-order-equation formulation is its easiness to include tensor permittivity in the waveguide structure. One useful aspect of directly obtaining six field components from the waveguide analysis lies in the combined application of the PSFD and PSTD methods in analyzing or simulating some device structures involving waveguide input. The complete profiles of the six field components of the input waveguide eigenmode can be readily used as the input functions to the PSTD computation with the same sub-domain mesh arrangement considered in the waveguide-mode calcuation and the time-domain simulation.

One key technique utilized in the present formulation is the same penalty scheme formulated in [24] for treating interface boundary conditions between adjacent sub-domains although we make the generalization here by implementing the stretched coordinate PML. Note that in the PSFD method of [21], directly matching interface conditions was employed. As discussed also in Subsection V.B in [33] which reported a PSFD method for solving scattering problems, the penalty scheme provides an edge-by-edge approach to impose interface conditions between sub-domains and it avoids the problematic issue of specifying a unique normal vector at a vertex point of a sub-domain by specifying two normal vectors at the vertex point using the nornmal vectors on the edges that intersect at the vertex. Every vertex point is thus enforced with two penalty interface conditions. We have found that the numerical convergence behavior through this penalty treatment appears to be better than that of [21] using the direct matching of interface conditions. One example is the analysis of the $p = 3$ mode shown in Table VI of the six-air-hole waveguide. Some comparison between the analysis results of [19] and [21] for this mode was discussed in Section V of [19], which showed an agreement not as superior as that betweem those of [19] and this work.

ACKNOWLEDGMENT

The authors would like to thank the National Center for High-Performance Computing in Hsinchu, Taiwan, the Academia Sinica Computing Center in Taipei, Taiwan, and the Computer and Information Networking Center at National Taiwan University for providing useful computing resources.

REFERENCES

[1] A. Yariv and P. Yeh, *Photonics: Optical Electronics in Modern Communications*, 6th ed. New York, NY, USA: Oxford Univ. Press, 2007.
[2] J. C. Knight, T. A. Birks, P. St, J. Russell, and D. M. Atkin, "All-silica single-mode optical fiber with photonic crystal cladding," *Opt. Lett.*, vol. 21, pp. 1547–1549, 1996.
[3] T. A. Birks, J. C. Knight, P. St, and J. Russell, "Endlessly single-mode photonic crystal fiber," *Opt. Lett.*, vol. 22, pp. 961–963, 1997.
[4] P. St and J. Russell, "Photonic crystal fibers," *Science*, vol. 299, pp. 358–362, 2003.
[5] Y. H. Chen and Y. T. Huang, "Coupling efficiency analysis and control of dual antiresonant reflecting optical waveguides," *J. Lightw. Technol.*, vol. 14, pp. 1507–1513, June 1996.
[6] C. H. Lai, B. You, J. Y. Lu, T. A. Liu, J. L. Peng, C. K. Sun, and H. C. Chang, "Modal characteristics of antiresonant reflecting pipe waveguides for terahertz waveguiding," *Opt. Exp.*, vol. 18, pp. 309–322, Jan. 2010.
[7] M. A. Duguay, Y. Kokubun, and T. L. Koch, "Antiresonant reflecting optical waveguides in SiO_2-Si multilayer structures," *Appl. Phys. Lett.*, vol. 49, pp. 13–15, 1986.
[8] N. Marcuvitz, "On field representations in terms of leaky modes or eigenmodes," *IRE Trans. Antennas Propagat.*, vol. 4, pp. 192–194, 1956.
[9] J. Hu and C. R. Menyuk, "Understanding leaky modes: Slab waveguide revisited," *Adv. Opt. Photon.*, vol. 1, pp. 58–106, 2009.
[10] A. A. Oliner, "Historical perspectives on microwave field theory," *IEEE Trans. Microw. Theory Tech.*, vol. MTT-32, pp. 1022–1045, 1984.
[11] J. P. Berenger, "A perfectly matched layer for the absorption of electromagnetic waves," *J. Comput. Phys.*, vol. 114, pp. 185–200, Feb. 1994.
[12] Z. Zhu and T. G. Brown, "Full-vectorial finite-difference analysis of microstructured optical fibers," *Opt. Exp.*, vol. 10, no. 17, pp. 853–864, Aug. 2002.
[13] C. P. Yu and H. C. Chang, "Yee-mesh-based finite difference eigenmode solver with PML absorbing boundary conditions for optical waveguides and photonic crystal fibers," *Opt. Exp.*, vol. 12, pp. 6165–6177, 2004.
[14] W. P. Huang, C. L. Xu, W. Lui, and K. Yokoyama, "The perfectly matched layer boundary condition for modal analysis of optical waveguides: Leaky mode calculations," *IEEE Photon. Technol. Lett.*, vol. 8, pp. 652–654, May 1996.
[15] Y. Tsuji and M. Koshiba, "Guided-mode and leaky-mode analysis by imaginary distance beam propagation method based on finite element scheme," *J. Lightw. Technol.*, vol. 18, pp. 618–623, 2000.
[16] S. Selleri, L. Vincetti, A. Cucinotta, and M. Zoboli, "Complex FEM modal solver of optical waveguides with PML boundary conditions," *Opt. Quantum Electron.*, vol. 33, pp. 359–371, 2001.
[17] T. P. White, B. T. Kuhlmey, R. C. McPhedran, D. Maystre, G. Renversez, C. M. de Sterke, and L. C. Botten, "Multipole method for microstructured optical fibers," *I. Formulation J. Opt. Soc. Amer. B*, vol. 19, pp. 2322–2330, Oct. 2002.
[18] T. P. White, B. T. Kuhlmey, R. C. McPhedran, D. Maystre, G. Renversez, C. M. de Sterke, and L. C. Botten, "Multipole method for microstructured optical fibers. II. implementation, and results," *J. Opt. Soc. Amer. B*, vol. 19, pp. 2331–2340, Oct. 2002.
[19] W. T. Lu and Y. Y. Lu, "Efficient boundary integral equation method for photonic crystal fibers," *J. Lightw. Technol.*, vol. 30, pp. 1610–1616, June 1, 2012.

[20] C. C. Huang, "Numerical calculations of ARROW structures by pseudospectral approach with Mur's absorbing boundary conditions," *Opt. Exp.*, vol. 14, pp. 11631–11652, Nov. 2006.
[21] P. J. Chiang and H. C. Chang, "A high-accuracy pseudospectral full-vectorial leaky optical waveguide mode solver with carefully implemented UPML absorbing boundary conditions," *Opt. Exp.*, vol. 19, pp. 1594–1608, Jan. 2011.
[22] P. J. Chiang, C. P. Yu, and H. C. Chang, "Analysis of two-dimensional photonic crystals using a multidomain pseudospectral method," *Phys. Rev. E*, vol. 75, pp. 026703–1-026703-14, Feb. 2007.
[23] P. J. Chiang, C. L. Wu, C. H. Teng, C. S. Yang, and H. C. Chang, "Full-vectorial optical waveguide mode solvers using multidomain pseudospectral frequency-domain (PSFD) formulations," *IEEE J. Quantum Electron.*, vol. 44, pp. 56–66, Jan. 2008.
[24] S. F. Chiang, B. Y. Lin, H. C. Chang, C. H. Teng, C. Y. Wang, and S. Y. Chung, "A multidomain pseudospectral mode solver for optical waveguide analysis," *J. Lightw. Technol.*, vol. 30, pp. 2077–2087, Jul. 1, 2012.
[25] W. J. Gordon and C. A. Hall, "Transfinite element methods: Blending-function interpolation over arbitrary curved element domains," *Numer. Math.*, vol. 21, pp. 109–129, 1973.
[26] C. H. Teng, B. Y. Lin, H. C. Chang, H. C. Hsu, C. N. Lin, and K. A. Feng, "A Legendre pseudospectral penalty scheme for solving time-domain Maxwell's equations," *J. Sci. Comput.*, vol. 36, pp. 351–390, Sept. 2008.
[27] W. C. Chew and W. H. Weedon, "A 3-D perfectly matched medium from modified Maxwell's equations with stretched coordinates," *Microw. Opt. Tech. Lett.*, vol. 7, pp. 599–604, Sept. 1994.
[28] A. Taflove and S. C. Hagness, *Computational Electrodynamics: The Finite-Difference Time-Domain Method*, 3rd ed. Norwood, MA, USA: Artech House, 2005.
[29] B. M. A. Rahman and J. B. Davies, "GaAs/GaAlAs rib waveguides," *Proc. Inst. Elect. Eng. pt. J.*, vol. 132, pp. 349–353, June 1985.
[30] P. Bienstman, S. Selleri, L. Rosa, H. P. Uranus, W. C. L. Hopman, R. Costa, A. Melloni, L. C. Andreani, J. P. Hugonin, P. Lalanne, D. Pinto, S. S. A. Obayya, M. Dems, and K. Panajotov, "Modelling leaky photonic wires: A mode solver comparison," *Opt. Quantum Electron.*, vol. 38, pp. 731–759, 2006.
[31] M. J. Adams, *An Introduction to Optical Waveguides*. New York, NY, USA: Wiley, 1981.
[32] G. R. Hadley, "High-accuracy finite-difference equations for dielectric waveguide analysis II: Dielectric corners," *J. Lightw. Technol.*, vol. 20, pp. 1219–1231, 2002.
[33] C. Y. Wang, S. Y. Chung, C. H. Teng, J. K. Wang, C. P. Chen, and H. C. Chang, "A high-accuracy multidomain Legendre pseudospectral frequency-domain method with penalty scheme for solving scattering and coupling problems of nano-cylinders," *J. Lightw. Technol.*, vol. 31, pp. 768–778, 2013.

Chih-Yu Wang received the B.S. degree from the Department of Engineering Science, National Cheng Kung University, Taiwan, in 2004, and the M.S. and Ph.D. degrees from the Graduate Institute of Electronics Engineering, National Taiwan University, Taiwan, in 2006 and 2012, respectively.

Her current research interests include the pseudospectral electromagnetics modeling in frequency domain.

Hsuan-Hao Liu was born in Hsinchu, Taiwan, R.O.C., on June 6, 1970. He received the diploma in mechanical engineering from National Taipei Institute of Technology, Taipei, Taiwan, in 1991, and the M.S. degree in mechanical engineering from Chung Yuan Christian University, Taoyuan, Taiwan, in 1995.

From 1995 to 1998 he was a piping engineer with CTCI Corporation in Taipei, Taiwan, where he worked on piping drafting design and piping stress analysis. From 1988 to 2001 he was a vice-engineer in piping engineering department at FU-TAI Engineering Co., Ltd., Taipei, Taiwan, where he worked on piping stress analysis and support design.

He is currently a Ph.D. candidate in the Computational Photonics and Electromagnetics Laboratory of the Graduate Institute of Photonics and Optoelectronics at National Taiwan University, Taipei, Taiwan. His research interests include finite element analysis of Photonic crystal fibers and anisotropic optical waveguides, numerical analysis of characteristic equations, fast algorithm for generate sparse matrices, and finite element mesh generation from CAD model.

Shih-Yung Chung received the B.S. degree from the Department of Electrical Engineering, National Cheng Kung University, Taiwan, in 2004, and the M.S. and Ph.D. degrees from the Graduate Institute of Electronics Engineering, National Taiwan University, Taiwan, in 2006 and 2012, respectively.

His current research interests include the electromagnetic simulations using the pseudospectral time domain method.

Chun-Hao Teng was born in Tainan, Taiwan, on February 14, 1970. He received the diploma in mechanical engineering from National Taipei Institute of Technology, Taipei, Taiwan, in 1990, and the M.S. degree in mechanical engineering from Clarkson University, Potsdam, NY, in 1996, and the M.S. and Ph.D. degrees in applied mathematics from Brown University, Providence, RI, in 2001. From 2003 to 2009 he was an Assistant Professor in the Department of Mathematics at National Cheng Kung University, Tainan, Taiwan. He is currently an Assistant Research Fellow at Center of Mathematical Modeling and Scientific Computing, National Chiao Tung University, Hsin-chu, Taiwan. His research interests are the developments and applications of high-order numerical methods for partial differential equations.

Chung-Ping Chen (M'96) received the B.S. degree in computer science and information engineering from National Chiao-Tung University, Hsinchu, Taiwan, in 1990, and the M.S. and Ph.D. degrees in computer science from the University of Texas, Austin, in 1996 and 1998, respectively. From 1996 to 1999, he was with Strategic Computer-Aided Design (CAD) Labs, Intel Corpo-ration, Hillsboro, OR, as a Senior CAD Engineer. Since 1999, he has been an Assistant Professor with the Department of Electrical and Computer Engineering, University of Wisconsin, Madison. Since 2003, he has been an Associate Professor with the Electrical Engineering Department, National Taiwan University, Taipei. Currently, he is a Professor with the Graduate Institute of Electronics Engineering, Biomedical Electronics and Bioinfor-matics and Electrical Engineering Departments, National Taiwan University. His research interests include the areas of electronic design automation and BIO topics, including computer-aided design and microprocessor circuit design with an emphasis on interconnect and circuit optimization, circuit simulation, statistical design, and signal/power/thermal integrity analysis and optimization.

Dr. Chen received the D2000 Award from Intel Corporation and the National Sciences Foundation Faculty Early Career Development awards (CAREER) from 1999 to 2001, respectively. He also received the 2002 Special Interest Group on Design Automation/ACM Outstanding Young Faculty Award and the 2002 IBM Peter Schneider Faculty Development Award. He served the program committee and is an organizer of the Design Automation Conference, the International Conference on Computer-Aided Design, Design, Automation, and the Test in Europe Conference, the International Symposium on Physical Design, the Asia and South Pacific Design Automation Conference, the International Symposium on Quality Electronic Design, Synthesis and System Integration of Mixed Information, the VLSI/CAD Symposium, and the International Technology Roadmap for Semiconductors Conference.

Hung-Chun Chang (S'78-M'83-SM'00) was born in Taipei, Taiwan, Republic of China, on February 8, 1954. He received the B.S. degree from National Taiwan University, Taipei, R.O.C., in 1976, and the M.S. and Ph.D. degrees from Stanford University, Stanford, CA, in 1980 and 1983, respectively, all in electrical engineering.

From 1978 to 1984, he was with the Space, Telecommunications, and Radioscience Laboratory of Stanford University. In August 1984, he joined the faculty of the Electrical Engineering Department of National Taiwan University, where he is currently a Distinguished Professor. He was the NTU Himax Chair Professor during 2011. He served as Vice-chairman of the EE Department from 1989 to 1991, and Chairman of the newly-established Graduate Institute of Electro-Optical Engineering at the same University from 1992 to 1998. His current research interests include the electromagnetic theory, design, and application of photonic structures and devices for fiber optics, integrated optics, optoelectronics, nanophotonics, and plasmonics.

Dr. Chang served as the IEICE (Japan) Overseas Area Representative in Taipei from 2002 to 2007. He is a Fellow of the Optical Society of America and the Electromagnetics Academy.